Article

Cell Stem Cell

Dynamic Reorganization of Chromatin Accessibility Signatures during Dedifferentiation of Secretory Precursors into Lgr5+ Intestinal Stem Cells

Graphical Abstract

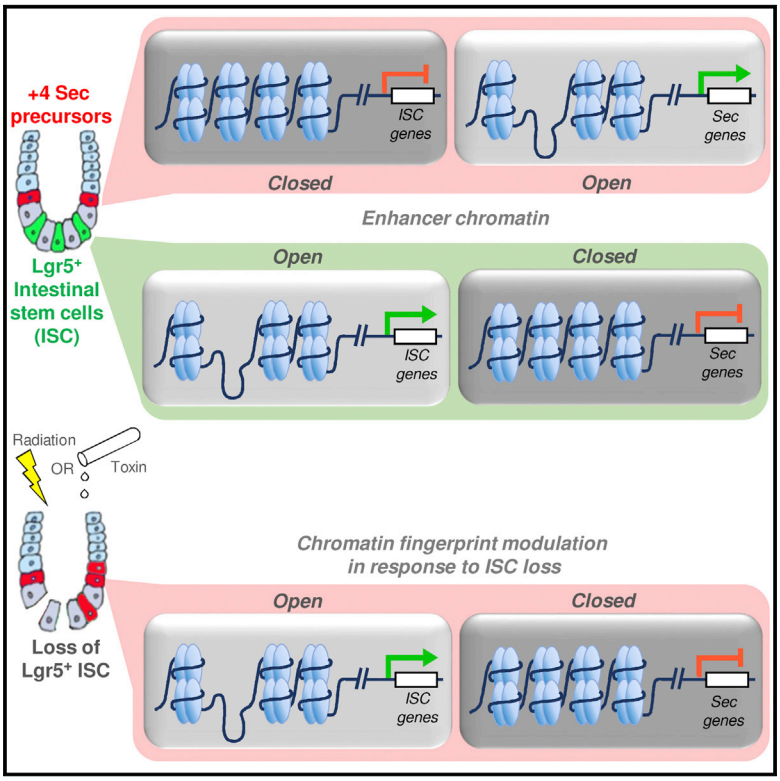

Highlights

- *Bmi1*^{Gfp} cells are endocrine cells and not dedicated facultative stem cells
- CD69 and CD274 mark related goblet cell precursors that regenerate Lgr5^{+} ISCs
- CD69^{+}CD274^{+} and Bmi1^{GFP+} cells contain a unique signature of open chromatin sites
- Chromatin and RNA profiles of these cells shift to resemble Lgr5^{+} ISCs after injury

Authors

Unmesh Jadhav, Madhurima Saxena, Nicholas K. O'Neill, ..., Zachary Herbert, Kazutaka Murata, Ramesh A. Shivdasani

Correspondence

ramesh_shivdasani@dfci.harvard.edu

In Brief

Jadhav et al. identify an active enhancer signature that distinguishes Lgr5^{+} intestinal stem cells (ISCs) from Bmi1^{GFP+} and other secretory cells, including CD69^{+}CD274^{+} goblet cell precursors. These specialized cells dedifferentiate into Lgr5^{+} ISCs in response to stem cell attrition, which is accompanied by dynamic rearrangements in open chromatin signatures.

Jadhav et al., 2017, Cell Stem Cell *21*, 65–77
July 6, 2017
http://dx.doi.org/10.1016/j.stem.2017.05.001

Cell Stem Cell
Article

Dynamic Reorganization of Chromatin Accessibility Signatures during Dedifferentiation of Secretory Precursors into Lgr5+ Intestinal Stem Cells

Unmesh Jadhav,[1,2] Madhurima Saxena,[1,2] Nicholas K. O'Neill,[1] Assieh Saadatpour,[3,4] Guo-Cheng Yuan,[3,4,5] Zachary Herbert,[6] Kazutaka Murata,[1,2] and Ramesh A. Shivdasani[1,2,5,7,8,*]
[1]Department of Medical Oncology and Center for Functional Cancer Epigenetics, Dana-Farber Cancer Institute, Boston, MA 02215, USA
[2]Department of Medicine, Harvard Medical School, Boston, MA 02215, USA
[3]Department of Biostatistics and Computational Biology, Dana-Farber Cancer Institute, Boston, MA 02215, USA
[4]Harvard TH Chan School of Public Health, Boston, MA 02215, USA
[5]Harvard Stem Cell Institute, Cambridge, MA 02138, USA
[6]Molecular Biology Core Facility, Dana-Farber Cancer Institute, Boston, MA 02215, USA
[7]Department of Medicine, Brigham and Women's Hospital, Boston, MA 02215, USA
[8]Lead Contact
*Correspondence: ramesh_shivdasani@dfci.harvard.edu
http://dx.doi.org/10.1016/j.stem.2017.05.001

SUMMARY

Replicating Lgr5$^+$ stem cells and quiescent Bmi1$^+$ cells behave as intestinal stem cells (ISCs) in vivo. Disrupting Lgr5$^+$ ISCs triggers epithelial renewal from Bmi1$^+$ cells, from secretory or absorptive progenitors, and from Paneth cell precursors, revealing a high degree of plasticity within intestinal crypts. Here, we show that GFP$^+$ cells from *Bmi1^{GFP}* mice are preterminal enteroendocrine cells and we identify CD69$^+$CD274$^+$ cells as related goblet cell precursors. Upon loss of native Lgr5$^+$ ISCs, both populations revert toward an Lgr5$^+$ cell identity. While active histone marks are distributed similarly between Lgr5$^+$ ISCs and progenitors of both major lineages, thousands of *cis* elements that control expression of lineage-restricted genes are selectively open in secretory cells. This accessibility signature dynamically converts to that of Lgr5$^+$ ISCs during crypt regeneration. Beyond establishing the nature of Bmi1^{GFP+} cells, these findings reveal how chromatin status underlies intestinal cell diversity and dedifferentiation to restore ISC function and intestinal homeostasis.

INTRODUCTION

Self-renewal of the intestinal epithelium is sustained principally by Lgr5$^+$ stem cells that lie at the bottom of intestinal crypts and replicate daily (Barker et al., 2007). It is unclear if a separate pool of quiescent stem cells is dedicated to replenishing Lgr5$^+$ intestinal stem cells (ISCs) when necessary (Barker, 2014; Richmond et al., 2016; Sangiorgi and Capecchi, 2008; Takeda et al., 2011). Ambiguous expression domains of Cre recombinase in lineage-tracing studies and of putative molecular markers fuel the uncertainty. Chromatin states can shed useful light on cell populations and on the basis for ISC recovery after ablative injuries.

Ideas about a facultative pool of reserve ISCs originated in observations on rare cells that reside mainly in crypt tier 4 and retain S phase labels for long periods, indicating replicative quiescence (Potten, 1998). These label-retaining cells (LRCs) share many features (small numbers, locations near tier 4, and infrequent cell division; Sangiorgi and Capecchi, 2008; Yan et al., 2012) with GFP$^+$ cells in mice that express GFP from the *Bmi1* locus, *Bmi1^{Gfp}* (Hosen et al., 2007). Attesting to their stem cell potential, *Bmi^{Gfp}* cells generate colonies in culture and increase in number when Lgr5$^+$ ISCs are ablated in vivo (Sangiorgi and Capecchi, 2008; Yan et al., 2012), a circumstance in which a *Bmi1*-expressing population is the source of new ISCs (Tian et al., 2011). One problem in interpreting these data is that *Bmi1* is expressed throughout intestinal crypts, including Lgr5$^+$ ISC and transit-amplifying (TA) cells (Itzkovitz et al., 2011; Muñoz et al., 2012), in sharp contrast to the few GFP$^+$ cells found in *Bmi^{Gfp}* mice (Li et al., 2014; Yan et al., 2012). Therefore, although *Bmi1* is often regarded as a specific marker of quiescent ISCs, GFP$^+$ cells in *Bmi^{Gfp}* mouse intestines represent a subset of *Bmi1*-expressing cells (Itzkovitz et al., 2011; Li et al., 2014), and because TA cells may express Cre recombinase in *Bmi^{Cre}* mice, it is difficult to pinpoint the source of replenished Lgr5$^+$ ISCs by lineage tracing (Tian et al., 2011). Identification of crypt cells by chromatin states and new molecular markers may help resolve these open questions.

Damage to Lgr5$^+$ ISC triggers crypt regeneration not only from Bmi1$^+$ cells but also from specified enterocytes (Ent) and secretory (Sec) progenitors (Pros) (Tetteh et al., 2016; van Es et al., 2012). Even LRCs, which were previously thought to represent quiescent ISC (Potten, 1998) but are now recognized as precursors of terminal Paneth and some enteroendocrine (EE) cells, contribute to the salvage (Buczacki et al., 2013; Li et al., 2016). This considerable plasticity implies that diverse crypt cells either have similar chromatin states or efficiently overcome a chromatin barrier when recruited to dedifferentiate into ISCs. Judging by the active histone modifications H3K4me2 and H3K27ac, the *cis*-element profiles of Lgr5$^+$ ISC, Sec-Pro and Ent-Pro are strikingly similar (Kim et al., 2014). This similarity may explain divergence of the two intestinal lineages by lateral inhibition,

but it is unclear how it engenders crypt cell diversity, including *Bmi1*^{Gfp} cells.

Here, we show that *Bmi*^{Gfp} cells are preterminal EE cells and identify related goblet cell precursors that express CD69 and CD274. Neither population seems to represent a dedicated pool of quiescent ISCs, but both dedifferentiate rapidly in response to ablation of native ISCs. We identify thousands of genome sites where chromatin is selectively open in Sec-Pro, *Bmi*^{Gfp}, and CD69^{+}CD274^{+} cells, but not in ISCs or Ent-Pros. Although these sites lack strong histone activation marks, they are bona fide enhancers for Sec-restricted genes. Upon loss of native ISCs, the distinctive chromatin signature of *Bmi1*^{Gfp} and CD69^{+}CD274^{+} cells reverts dynamically toward that of Lgr5^{+} cells. This transition reflects the rapid breach of a chromatin barrier when specified crypt cells are enlisted to restore ISC function.

RESULTS

Bmi1^{Gfp} Cells Are Mature EE Cells and Not a Dedicated Pool of "Reserve" ISCs

In duodenal crypts in *Bmi*^{Gfp} mice (Hosen et al., 2007), GFP^{+} cells lie just above the Lgr5^{+} ISC and Paneth cell zone (Figure 1A). To determine the lineage of these GFP^{+} cells, we isolated them by flow cytometry (Figure S1A) and compared their RNA sequencing (RNA-seq) profiles to those of Lgr5^{+} ISCs (Barker et al., 2007), Sec-Pros isolated from wild-type crypts after pharmacologic inhibition of Notch signaling (van Es et al., 2005), and Ent-Pros from *Atoh1*$^{-/-}$ crypts (Kim et al., 2014) (Table S1; Figure S1B); high *Epcam* mRNA levels confirmed the epithelial origin of each population (Figure S1B). We also profiled Lgr5^{+} ISCs harvested from another mouse strain, *Lgr5*$^{Dtr\text{-}Gfp}$ (Tian et al., 2011) and Sec-Pros isolated after genetic disruption of Notch activity (Kim et al., 2014) (Figure S1C). Hundreds of transcripts were enriched or present exclusively in *Bmi1*^{Gfp} cells, such as the *Serpina1* cluster, transcription factors (TFs) of the Ets/Fli/Fev family, and especially genes known for EE cell expression (Figures 1B and S1D). In principal-component analysis (PCA), *Bmi1*^{Gfp} cells accounted for the bulk of variation (Figure 1C). Compared to the other populations, transcripts present selectively (>3-fold, $q < 0.05$) in *Bmi1*^{Gfp} cells were depleted in the "Cell cycle" category and enriched for "Quiescence" and "Targets of fusion transcription factor EWSR1-FLI1" (Figure S1E). Thus, *Bmi1*^{Gfp} cells have an mRNA profile distinct from Lgr5^{+} ISCs and crypt progenitors.

Because one prevalent view is that *Bmi*^{Gfp} cells represent quiescent ISCs that periodically replenish the pool of Lgr5^{+} ISC (Li et al., 2014; Richmond et al., 2016; Yan et al., 2012), we sought to determine their position within the crypt hierarchy. We used successive changes in mRNA expression to derive quantitative scores for every possible trajectory among stem, progenitor, and the abundant differentiated villus cell types: enterocytes and goblet cells (STAR Methods; Figure S1F). Among every possible model, those in which *Bmi*^{Gfp} cells spawn Lgr5^{+} ISCs or progenitors gave unfavorable scores; only a model where they originate in Sec-Pros gave a high positive score (Figure 1D). In line with this result, crypts lacking ATOH1, a TF required for Sec specification (Shroyer et al., 2007; Yang et al., 2001), were largely devoid of *Bmi1*^{Gfp} cells (Figures 1E and S1G).

Bmi1^{Gfp} cells lacked transcripts classically ascribed to goblet or Paneth cells; rather, they were enriched for canonical EE genes, with the hormone *Ghrelin* being particularly abundant and specific (Figure S2A). We therefore purified crypt EE and Paneth cells using flow cytometry for CD24 and *Ulex europaeus* agglutinin (Wong et al., 2012), verified the purity of various cell isolates by RT-PCR analysis of established lineage markers (Figure S2B), and profiled transcripts using RNA-seq (Table S1). Gene set enrichment analysis (GSEA) (Subramanian et al., 2005) and trajectory analysis indicated that *Bmi1*^{Gfp} cells are related most closely to EE cells (Figures 1F and S2C). Moreover, 91% of *Bmi*^{Gfp} cells showed high expression of the EE-specific marker CHGA (Figure 1G), and the population is enriched for RNAs encoding many hormones and TFs known to control EE cells (Figures S2D and S2E). These data reveal *Bmi1*^{Gfp} cells as non-replicating *ChgA*$^{+}$ EE cells, with high expression of hormone RNAs and *Neurod1* (compared to *Neurog3*), suggesting advanced differentiation (Li et al., 2012); our trajectory data suggest preterminal EE maturity (Figure S2C). *Bmi1*^{Gfp} cells thus do not seem to represent a dedicated pool of reserve ISCs, though they may when necessary dedifferentiate into Lgr5^{+} ISCs, like other precursors (Buczacki et al., 2013; Schwitalla et al., 2013; Tetteh et al., 2016; van Es et al., 2012; Westphalen et al., 2014). Notably, no crypt cells have been captured in the act of dedifferentiation.

Identification of Goblet Cell Precursors in Wild-Type Mouse Crypts

Because our goal was to capture such cells and examine transitional chromatin states, we sought next to identify potentially labile crypt populations in wild-type mice. Noting that some surface marker RNAs express at considerably higher levels in *Bmi1*^{Gfp} cells than in Lgr5^{+} ISCs (Figure S3A), we used flow cytometry to test expression of selected such proteins. CD69 and CD274 reproducibly marked ~9% (n = 7) of viable wild-type EPCAM^{+} crypt epithelial cells (Figure S3B). These proteins were rarely present alone, and both flow cytometry and immunofluorescence robustly identified a CD69^{+}CD274^{+} cell population that localized in crypt positions above the Paneth-ISC zone (Figures 2A, 2B, and S3B). Although *Cd69* and *Cd274* mRNAs are absent from Lgr5^{+} ISCs (Figure S3A), to exclude any potential overlap of cell types, we treated *Lgr5*$^{Dtr\text{-}Gfp}$ mice with four doses of diphtheria toxin (Tian et al., 2011) and harvested crypt cells the following day. Lgr5^{+} ISCs were lost after toxin treatment as expected (Figure S3C), whereas CD69^{+}CD274^{+} cells remained (Figure 2B), indicating that the populations are distinct. Moreover, few CD69^{+}CD274^{+} cells took up bromodeoxyuridine (Figure 2C), revealing that they are largely quiescent. CD69^{+}CD274^{+} cells were absent from *Atoh1*$^{-/-}$ intestines and their mRNA profile matched that of Sec-Pro (Figure 2D), indicating that they belong to the Sec lineage.

Although *Cd69* and *Cd274* are expressed in *Bmi1*^{Gfp} cells (Figure S3A), analysis of all mRNAs present at different levels in various Sec populations suggested that fluorescence-activated cell sorting (FACS)-sorted *Bmi1*^{Gfp} and CD69^{+}CD274^{+} cells are distinct entities. *K*-means clustering of differential mRNAs confirmed the close relation of *Bmi1*^{Gfp} to EE cells and revealed that CD69^{+}CD274^{+} cells most resemble goblet cells (Figure 2E). Indeed, the CD69^{+}CD274^{+} population lacks *Chga*, *Cck*, *Ghrl*,

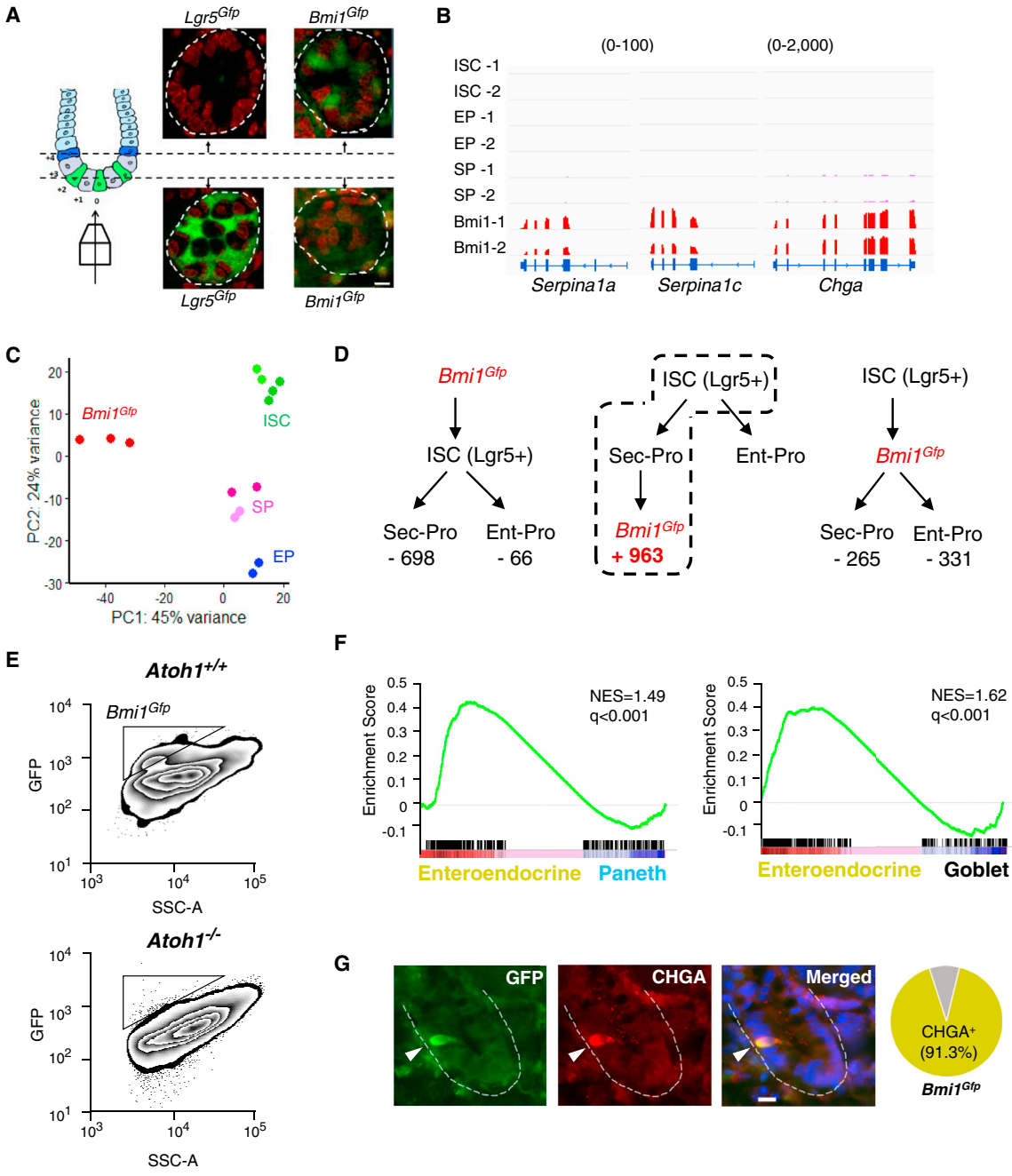

Figure 1. *Bmi1*^{Gfp} Cells Belong to the EE Lineage

(A) Confocal microscopy on optically cleared tissue confirms the distinct locations of Lgr5^{+} ISCs (crypt base) and *Bmi1*^{Gfp} cells (higher crypt tiers). Scale bar, 10 μm.

(B) RNA-seq tracks illustrating *Bmi1*^{Gfp} cell-restricted genes, including the *Serpina1* cluster and EE marker *Chga*.

(C) Principal-component analysis (PCA) of mRNA differences among crypt cells. *Bmi1*^{Gfp} cells are distinct from others along principal component (PC1). Three ISC samples were derived from *Lgr5*^{Gfp} and two from *Lgr5*^{Dtr} mice. Two Sec-Pro samples each were isolated after pharmacologic or genetic Notch inhibition. SP, Sec-Pro; EP, Ent-Pro.

(D) Cell trajectory models based on global mRNA levels impute *Bmi1*^{Gfp} cells as descendants of Sec-Pros. Scores reflect monotonic expression changes for each trajectory.

(E) Flow cytometry plots showing lack of *Bmi1*^{Gfp} cells in *Atoh1*$^{-/-}$ crypts.

(F) Gene set enrichment analysis (GSEA) of the 500 highest expressed genes in *Bmi1*^{Gfp} cells in relation to EE, Paneth, and goblet cell transcriptomes.

(G) Co-expression of GFP and CHGA in *Bmi1*^{Gfp} duodenal cells (n = 165 cells). Representative individual and merged fluorescence images are displayed. Scale bar, 20 μm.

See also Figures S1 and S2.

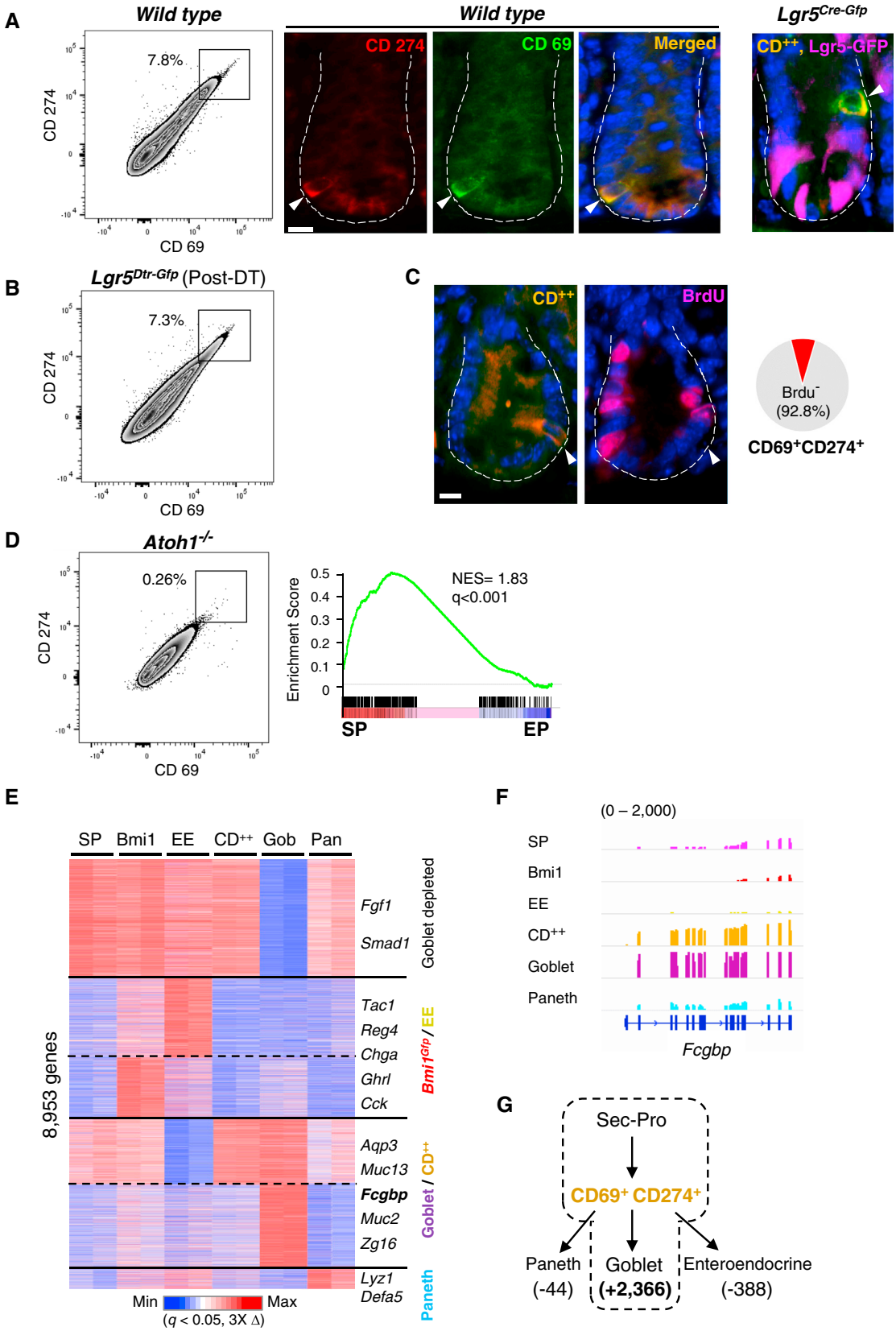

(legend on next page)

and other abundant EE transcripts but selectively expresses known goblet cell genes (Pelaseyed et al., 2014; Zhu et al., 2016) (Figures 2E, 2F, and S3D). mRNA flux in the Sec lineage also gave the best score for the trajectory Sec-Pro → CD69$^+$CD274$^+$ cells → goblet cells (Figure 2G). Thus, CD69$^+$CD274$^+$ crypt cells represent a wild-type Sec population that is anatomically close to the ISC zone and strongly biased toward goblet cell differentiation.

mRNA Changes Identify Sec Cells in the Act of Dedifferentiation

Lineage tracing studies have elegantly revealed the origins of new Lgr5$^+$ ISC, generally days or weeks after injury to the native ISC pool (Barker, 2014). To detect such a transition in *Bmi1*^{Gfp} cells, we confirmed that 10 Gy whole-body γ-irradiation eliminates Lgr5$^+$ ISCs, as reported previously (Metcalfe et al., 2014), delivered this dose to *Bmi1*^{Gfp} mice, and isolated GFP$^+$ cells 36 hr later. Because the *Lgr5* locus is unmodified in these mice, GFP$^+$ cells originate exclusively in the *Bmi1*^{Gfp} population, and the short interval enabled capture of cells during their possible conversion to GFP$^-$ ISCs. Irradiated *Bmi1*^{Gfp} mice yielded three to four times more GFP$^+$ cells than unirradiated controls, as reported previously (Tian et al., 2011; Yan et al., 2012). After irradiation, *Bmi1*^{Gfp} cells showed mRNA features that normally signify either *Bmi1*^{Gfp} cells or Lgr5$^+$ ISCs (but not both); reduced levels of otherwise abundant and specific transcripts, such as the *Serpina1* cluster, were particularly evident (Figure 3A). RT-PCR analysis of changes in *Bmi1*^{Gfp} cells, compared to bulk crypt cells isolated before and after irradiation, demonstrated the specificity of this response (Figures 3B and S3E). Thus, radiation-induced loss of native ISCs forces *Bmi1*^{Gfp} cells into a genuine transition.

To determine whether CD69$^+$CD274$^+$ cells also can revert into ISCs, we were sensitive to the possibility that, beyond eliminating Lgr5$^+$ cells, γ-irradiation might directly affect other cell types. We therefore treated *Lgr5*$^{Dtr\text{-}Gfp}$ mice with diphtheria toxin, which ablates Lgr5$^+$ ISCs selectively (Tian et al., 2011). We verified that Lgr5$^+$ ISCs begin to return 2 days after the last dose of toxin and harvested CD69$^+$CD274$^+$ cells 1 day after this final dose, i.e., while GFP$^+$ cells are absent from the crypt (Figure S3C). We observed attenuation of CD69$^+$CD274$^+$ cell-specific genes and clear activation of genes ordinarily expressed only in ISCs (Figure 3C). PCA placed post-toxin cells in a discrete group, related more closely than parental CD69$^+$CD274$^+$ cells to Lgr5$^+$ ISC (Figure 3D), and at least half among a panel of 12 stringently defined ISC-specific genes (Muñoz et al., 2012) were reproducibly activated in CD69$^+$CD274$^+$ cells during ISC recovery (Figures 3E and 3F). Similar gain of ISC-specific transcripts was not evident in bulk crypt cells isolated before and after toxin treatment (Figures 3G and S3F). Thus, after ISC loss, mRNA changes in CD69$^+$CD274$^+$ cells represent another authentic and active transition toward ISCs. Of note, only 5 and 33 of the hundreds of transcripts altered after ISC loss in CD69$^+$CD274$^+$ and *Bmi1*^{Gfp} cells, respectively, correspond to the 212 genes linked to "Cell proliferation" in Gene Ontology.

Selectively Open Chromatin Distinguishes Sec Cell Populations from Lgr5$^+$ ISCs

These changes in gene expression and cell identity must have a basis in chromatin. We have reported, however, that the active histone marks H3K4me2 and H3K27ac appear at the same genome sites in specified Sec- and Ent-Pros (Kim et al., 2014). To confirm these findings at nucleosome resolution, we digested chromatin from Pro cells with micrococcal nuclease and repeated chromatin immunoprecipitation sequencing (ChIP-seq) for these histone marks (Table S1). Global analysis of the data confirmed near identity of Sec- and Ent-Pro profiles (Figure S4A), as reflected in the findings at the lineage-restricted *Notch1* and *Dll1* loci (Figure 4A). These data underscore the need to identify a basis other than active histone marks for differentiation and dedifferentiation of intestinal crypt cells. Because the numbers of *Bmi1*^{Gfp} or CD69$^+$CD274$^+$ cells are too small for robust ChIP, we used the assay for transposase-accessible chromatin with high-throughput sequencing (ATAC-seq) (Buenrostro et al., 2013) to identify areas of open chromatin (Table S1). Replicate samples gave concordant ATAC signals (Figure S4B) that coincided with promoters and putative enhancers and readily distinguished cell types (Figure 4B). Unsupervised hierarchical clustering of the ~50,000 ATAC sites we identified in one or more populations classified *Bmi1*^{Gfp} and CD69$^+$CD274$^+$ cells as distinct from Lgr5$^+$ ISCs or Ent-Pros and most similar to Sec-Pros (Figure 4C). Because promoters vary little across cell types (Heintzman et al., 2009), we focused on the ~41,000 putative enhancers (sites >1 kb from transcription start sites). *k*-means clustering (Figures S4C and S4D) revealed three main groups: sites with similar ATAC signals in all five cell types (group 1, ~10,000 sites), regions that gave stronger signals in ISCs and Ent-Pros (group 2, ~16,000 sites), and those that were only apparent (or strongest) in the three Sec populations (group 3, ~14,800 sites) (Figure 4D).

Nearly all the candidate enhancers in groups 1 and 2 carry H3K4me2 and/or H3K27ac in both progenitors and Lgr5$^+$ ISCs

Figure 2. CD69 and CD274 Mark a Crypt Sec Population of Goblet Cell Precursors

(A) Wild-type CD69$^+$CD274$^+$ cell fractions detected by flow cytometry with both antibody (Ab) (n = 5) and by immunofluorescence (IF), which showed co-expression in cells lying just above the crypt base. Scale bar, 10 μm. IF in untreated *Lgr5*$^{Dtr\text{-}Gfp}$ mice shows their location just above the Lgr5$^+$ ISC zone.

(B) Elimination of Lgr5$^+$ ISC in *Lgr5*$^{Dtr\text{-}Gfp}$ mouse intestines by diphtheria toxin (DT) did not remove CD69$^+$CD274$^+$ cells (n = 4).

(C) Representative IF of serial tissue sections showing non-overlapping signals from CD69$^+$CD274$^+$ cells and bromodeoxyuridine (BrdU)$^+$ cells. Scale bar, 10 μm.

(D) Absence of CD69$^+$CD274$^+$ cells by flow cytometry in *Atoh1*$^{-/-}$ intestines (n = 3), and GSEA of the 500 highest expressed genes in wild-type mice reveals a closer match with Sec-Pros (SPs) than with Ent-Pros (EPs).

(E) Relative mRNA levels of 8,953 genes differentially expressed (>3-fold, $q < 0.05$) among secretory cell types in duplicate, grouped by unsupervised *k*-means clustering ($k = 6$, as determined by the gap statistic).

(F) RNA-seq tracks showing expression of goblet cell-specific *Fcgbp*.

(G) Comparative cell trajectory modeling based on global RNA expression imputes CD69$^+$CD274$^+$ cells as goblet cell precursors.

See also Figure S3.

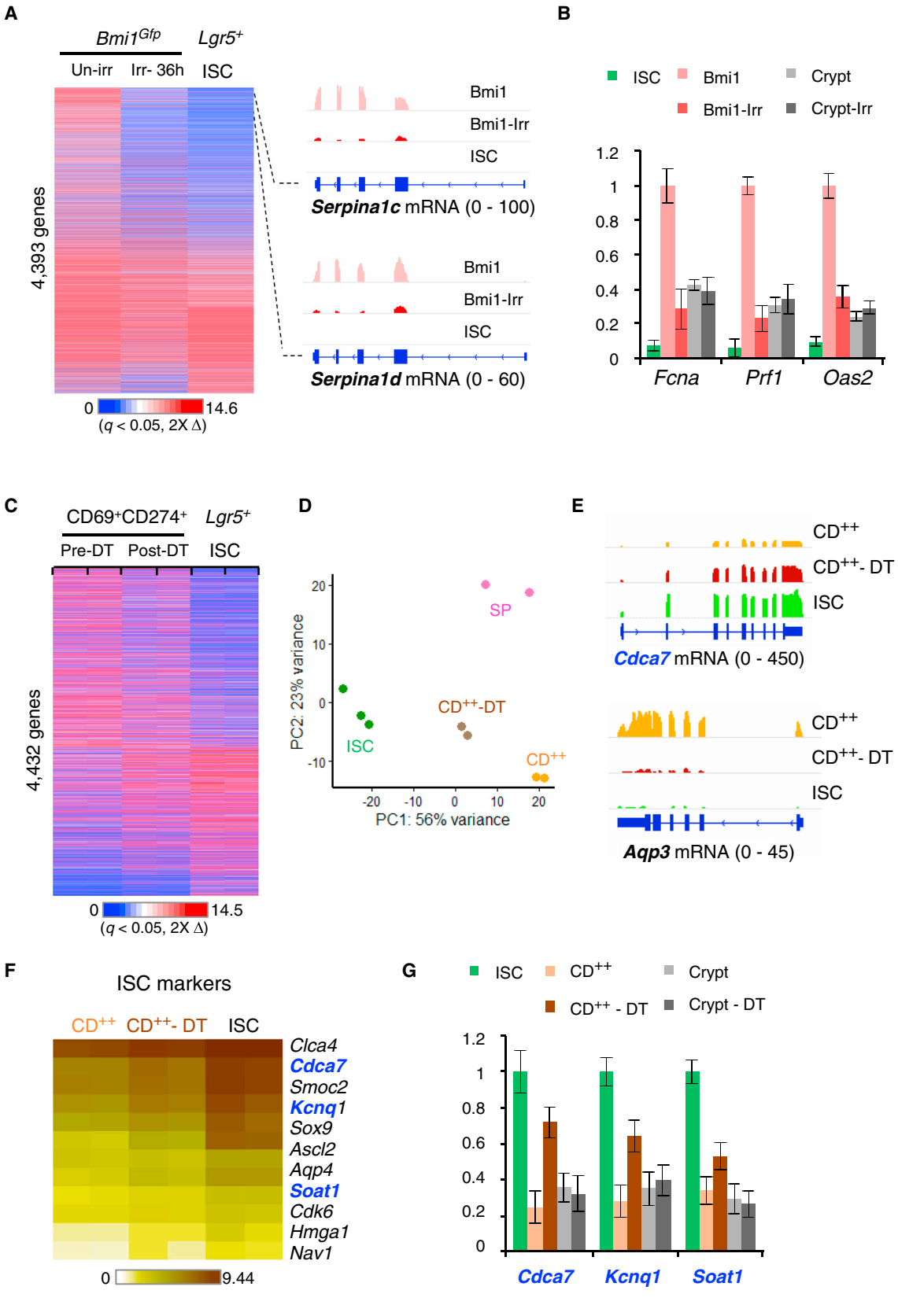

(legend on next page)

(Figure 4D) and correspond to sites previously identified (Kim et al., 2014) by ChIP-seq for these active histone marks (Figure S4D). In contrast, regions in group 3 lack these marks and had therefore eluded detection previously. Sites open in Ent-Pros gave ATAC signals of comparable strength in Lgr5$^+$ ISCs, while chromatin access in CD69$^+$CD274$^+$ and *Bmi1*^{Gfp} cells resembled Sec-Pros (Figures 4D and 4E). This dominance of group 2 enhancers in Lgr5$^+$ ISCs and Ent-Pros, and of group 3 enhancers in the Sec lineage, is striking.

Regions of Selectively Open Chromatin in Sec Cells Represent Bona Fide Active *cis* Elements

Many active embryonic stem cell (ESC) enhancers have open chromatin but lack H3K27ac (Pradeepa et al., 2016), similar to group 3 sites in Sec cells (Figures 4D and S4D). Because such discrepancy between open chromatin and active histone marks is not appreciated widely in adult tissues, we asked if group 3 sites correspond to functional enhancers. ChIP-seq for the poised enhancer feature H3K4me1 (Figure S5A) (Shlyueva et al., 2014) gave stronger signals than the other marks, revealing H3K4me1 at many group 3 sites (Figures 5A and 5B). Of note, this mark also appeared at the same sites in Sec- and Ent-Pros; thus, the three histone marks associated with enhancer activity showed high concordance with ATAC signals across all cell types (Figure S5B). In further support of the bona fides of group 3 regions, ATAC signals are comparable to those in group 2 (Figures 4D and 4E), many of the sites are also accessible in lymphocytes (Lara-Astiaso et al., 2014), and nearby genes are as or more enriched for distinctive biological processes than those near well-marked enhancers in group 2 (Figure S5C). Moreover, while group 2 regions are enriched in motifs for known enterocyte-active factors (HNF4A and CDX2; Verzi et al., 2010), those in group 3 are equally enriched for distinct TF sequence motifs (ETS, FLI, FEV, and RUNX; Figure S5C). FEV in particular is expressed in rare crypt cells that lie just above the ISC zone, coincident with CD69$^+$ cells (Figure 5C), and RNA expression and ATAC signals for several TF genes in the FL1/FEV family are specific to Sec cells (Figure 5D). Finally, many loci, including *CD69*, showed Sec cell-restricted ATAC- and RNA-seq signals (Figure 5E), much as the signals at *Lgr5* were restricted to ISC (Figure S5D). To assess global trends in cell-restricted gene control, we applied a GSEA approach (Subramanian et al., 2005) to relate cell-type-specific transcripts (Figure 2E) to sites of open chromatin. While no set of specific genes was preferentially located near group 2 regions (Figure S5E), those enriched in *Bmi1*^{Gfp} cells and Sec-Pros were preferentially located near group 3 sites (Figure 5F). Thus, these areas of selective chromatin access are authentic enhancers for Sec-specific genes associated with distinct TFs and biologic functions.

Dynamic Transitions of Open Chromatin in Dedifferentiating Crypt Sec Cells

The nearly identical profiles of chromatin access in Lgr5$^+$ ISC and Ent-Pro (Figure 4D) imply a low barrier for the latter cells to replace lost Lgr5$^+$ ISCs, as occurs after γ-irradiation (Tetteh et al., 2016). However, *Dll1*$^+$ Sec-Pros (van Es et al., 2012) and label-retaining cells (Buczacki et al., 2013) also can replace lost Lgr5$^+$ ISCs, and *Bmi1*^{Gfp} and CD69$^+$CD274$^+$ cells both transition toward Lgr5$^+$ ISCs (Figure 3). The abundance of additional enhancers (group 3) in the Sec lineage implies that these cells must traverse this chromatin barrier when they dedifferentiate.

To witness chromatin dynamics during dedifferentiation, first we harvested *Bmi1*^{Gfp} cells 24 hr and 36 hr after 10 Gy γ-irradiation and compared the ATAC profiles to those of *Bmi1*^{Gfp} cells from unirradiated mice. Unsupervised clustering based on ATAC signals in all populations placed the post-radiation cells closer to Lgr5$^+$ ISCs than to the parental cells (Figure 6A). Post-radiation cells showed low ATAC signal at many group 3 regions that are unequivocally accessible in unirradiated *Bmi1*^{Gfp} cells and stronger signals at many ISC-specific sites (Figure 6B); the latter effect may be dampened by the inability to capture fully reverted cells, whose diminished *Bmi1* expression would reduce GFP to sub-threshold levels. We then compared chromatin from CD69$^+$CD274$^+$ cells isolated before and after ablation of ISC in *Lgr5*^{Dtr} mice. Again, the baseline profile of accessible chromatin shifted dramatically to that of Lgr5$^+$ ISCs, showing loss of group 3 and gain of group 2 enhancers (Figures 6C and 6D). Although we isolated cells based on CD69 and CD274, which are restricted to Lgr5$^-$ cells (Figures 2B and S3A), the gain of group 2 enhancers was extensive, in agreement with activation of genes usually restricted to Lgr5$^+$ ISCs (Figure 3D-F). Global analyses confirmed significant adaptive modulation of chromatin state during Sec cell dedifferentiation, irrespective of the cell source (*Bmi1*^{Gfp} or CD69$^+$274$^+$) or the mode of ISC attrition (Figures 6E and S6).

DISCUSSION

At least two mutually exclusive intestinal crypt cell types manifest stem cell behavior in vivo: cycling Lgr5$^+$ cells (Barker et al.,

Figure 3. Modulation of Gene Expression in *Bmi*^{Gfp} and CD69$^+$CD274$^+$ Cells upon Lgr5$^+$ ISC Loss

(A) mRNA changes in *Bmi*^{Gfp} cells before and after γ-irradiation. The 4,393 genes differentially expressed (>2-fold, $q < 0.05$) in Lgr5$^+$ and *Bmi*^{Gfp} cells are arranged in descending order of baseline differences; RNA levels in post-irradiated *Bmi*^{Gfp} cells are shown alongside. Representative RNA-seq tracks showing reduced levels of *Bmi*^{Gfp} cell-specific *Serpina1* transcripts.

(B) qRT-PCR analysis showing that changes in gene expression triggered by ISC loss occur in *Bmi*^{Gfp} and not all crypt cells (n = 3 each; error bars are SD from biological triplicates).

(C) mRNA changes in CD69$^+$CD274$^+$ cells (CD^{2+}) before and after ISC loss. The 4,432 genes differentially expressed (>2-fold, $q < 0.05$) in Lgr5$^+$ and CD^{2+} cells are arranged in descending order of differences, and RNA levels in CD^{2+} cells after diphtheria toxin (DT) are shown in the middle.

(D) PCA of mRNA modulation showing that, upon DT-induced ISC loss, CD^{2+} cells cluster away from native CD^{2+} and closer to ISCs.

(E) Representative RNA-seq data showing increase of ISC-specific (*Cdca7*) and reduction of goblet-specific (*Aqp3*) transcripts.

(F) Heatmap representation of 12 stringently defined ISC marker genes (Muñoz et al., 2012).

(G) qRT-PCR analysis showing selective gain of ISC maker genes in CD^{2+} cells compared to bulk populations of crypt cells (n = 3 each; error bars are SDs from biological triplicates).

See also Figure S3.

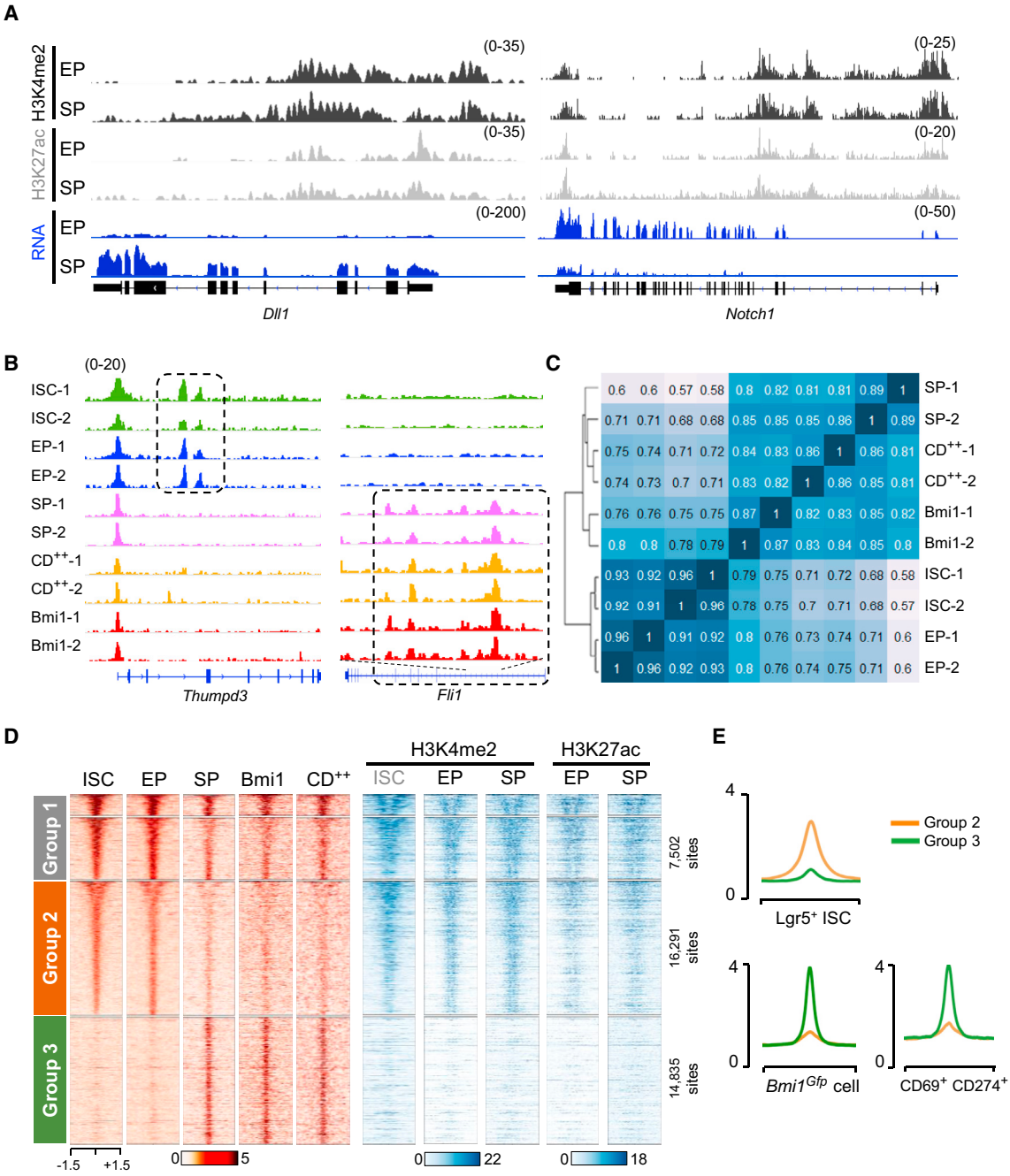

Figure 4. Distinctive Profile of Chromatin Access Separates Sec Cells, Including *Bmi*^{Gfp} and CD69^{+}CD274^{+}, from ISC and Ent Cells

(A) ChIP- and RNA-seq data tracks showing similar locations and strength of active enhancer marks H3K4me2 and H3K27ac along loci specifically expressed in Sec-Pros (SPs; *Dll1*) and Ent-Pros (EPs; *Notch1*).

(B) ATAC signal tracks from duplicates of each crypt cell type at loci that illustrate differential chromatin access.

(C) Matrix of Spearman correlation coefficients for global chromatin access derived from ATAC-seq data. Sec-Pro, *Bmi1*^{Gfp}, and CD^{2+} cells cluster separately from ISCs and Ent-Pros.

(D) Heatmaps showing *K*-means-derived grouping of 41,167 regions (>1 kb from TSSs) of ATAC- identified open chromatin alongside active histone marks (Chip-seq) at the same sites. ChIP data on ISCs were reported previously from sonicated chromatin (Kim et al., 2014); MNase-ChIP data on EPs and SPs are new to this study.

(E) Average ATAC signals at group 2 and group 3 enhancers in ISCs, *Bmi1*^{Gfp} cells, and CD^{2+} cells.

See also Figure S4.

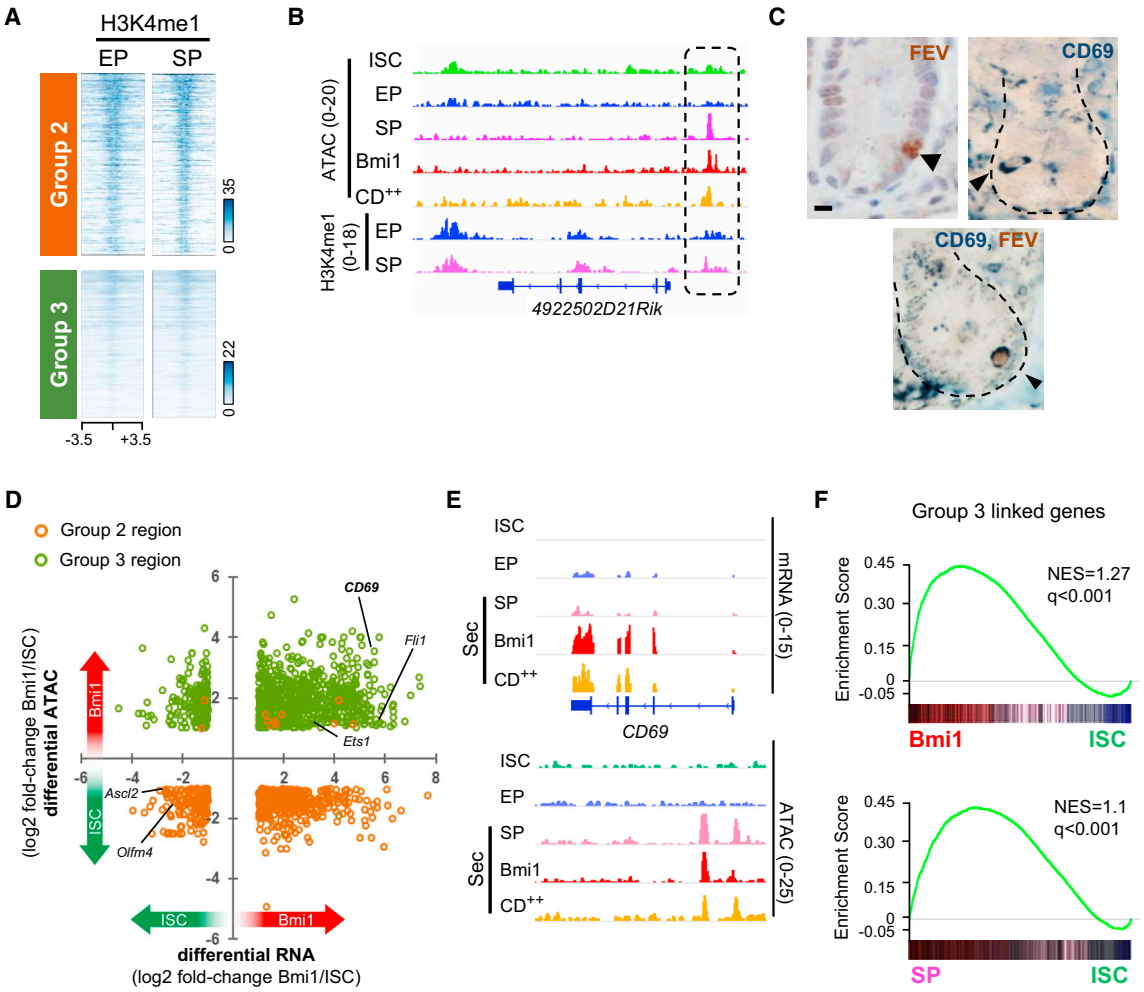

Figure 5. Chromatin Selectively Open in the Sec Lineage Controls Sec-Restricted Genes

(A) The 14,835 sites in group 3 show discernible H3K4me1, which is weaker than signals in group 3 but present at similar levels in Ent- and Sec-Pros.

(B) ATAC- and ChIP-seq data from each cell type at a representative locus demonstrating co-localization of open chromatin and H3K4me1 in non-promoter regions within group 3.

(C) Location of rare FEV^{+} and CD69^{+} cells in cells near crypt tier 4 (top, stained separately) and co-expression of both markers (bottom, stained simultaneously). Scale bar, 10 μm.

(D) Differential ATAC- and RNA-seq showing cell type specific association of open chromatin regions and gene expression.

(E) Illustrative ATAC- and RNA-seq tracks showing *Cd69* mRNA and open chromatin in a 3′ intron, both restricted to the Sec cell types SP, *Bmi1*^{Gfp}, and CD^{2+}.

(F) GSEA of genes located <25 kb from group 3 enhancers shows robust association with transcripts highly enriched in *Bmi1*^{Gfp} cells and Sec-Pros (SPs) relative to Lgr5^{+} ISCs. NES, normalized enrichment score.

See also Figure S5.

2007) and quiescent Bmi1^{hi} cells (Sangiorgi and Capecchi, 2008; Yan et al., 2012). In addition, loss of Lgr5^{+} ISCs induces dedifferentiation of both Sec and Ent precursors (Buczacki et al., 2013; Tetteh et al., 2016; van Es et al., 2012), which probably underlies injury-dependent conversion of *Bmi1*-expressing TA cells into ISCs (Tian et al., 2011). The basis for this exceptional plasticity among specialized crypt cells is unclear. Using open chromatin to shed light on this question, we show that ~15,000 selectively accessible genomic sites constitute a Sec lineage signature. These group 3 enhancers open when Sec cells differentiate from Lgr5^{+} ISCs, and they rapidly relinquish chromatin access when *Bmi1*^{Gfp} or wild-type CD69^{+}CD274^{+} cells dedifferentiate in the face of ISC loss. The reversible ATAC profile in Sec cells reveals dynamic modulation of lineage-specific chromatin access in vivo.

The locations and strength of active histone marks H3K4me1/2 and H3K27ac are strikingly similar in Sec- and Ent-Pros (Kim et al., 2014). These enhancer marks generally coincide with sites identified in assays for open chromatin, such as DNaseI hypersensitivity or ATAC (Buenrostro et al., 2013; Mercer et al., 2013). Thus, while the scant histone marks at Sec-specific enhancers explain why they were not detected previously, the disparity between chromatin access and active histones is atypical, especially in light of their regulatory activity.

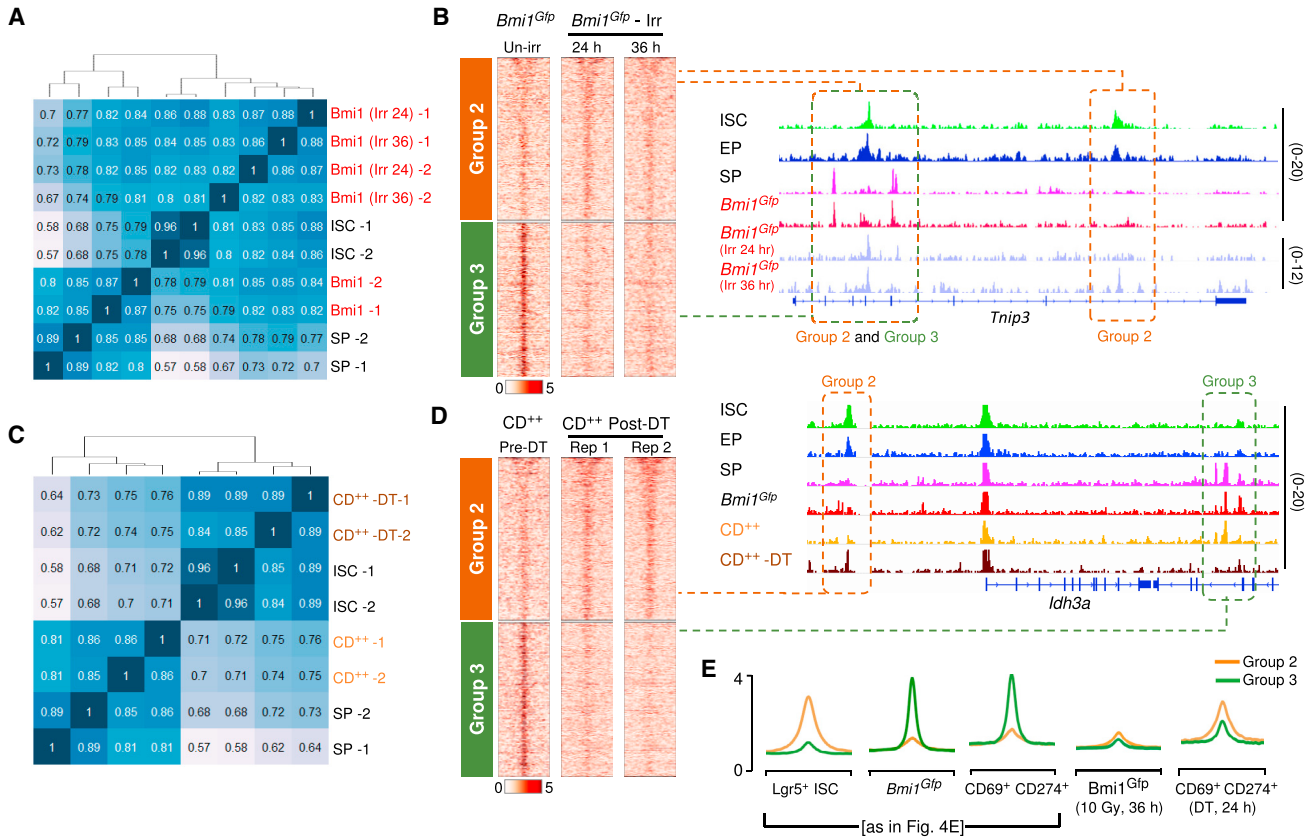

Figure 6. Dynamic Modulation of Chromatin Access in *Bmi*^{Gfp} and CD^{2+} Cells upon Loss of Lgr5^{+} ISCs

(A and C) Similarity matrices (Spearman correlation coefficients) for global chromatin access (ATAC-seq) in *Bmi*^{Gfp} cells (A) before and 24 hr and 36 hr after γ-irradiation, and in CD^{2+} cells (C) 24 hr after the last dose of diphtheria toxin (DT) in relation to other crypt populations. Both post-radiation GFP^{+} cells and post-DT CD^{2+} cells cluster with Lgr5^{+} ISCs, away from their respective parental populations.

(B and D) Widespread loss of ATAC signal at group 3 sites, with commensurate relative gain at many group 2 regions, in duplicate samples of *Bmi*^{Gfp} cells after γ-irradiation (B) and post-DT CD^{2+} cells (D). ATAC-seq tracks in each case illustrate losses and gains of open chromatin.

(E) Relative strengths of ATAC signals averaged across all group 2 and group 3 enhancers upon ISC loss in *Bmi*^{Gfp} and CD^{2+} cells. Aggregate profiles from wild-type cells (Figure 4E) are shown again for comparison.

See also Figure S6.

One possibility is that the sites acquire canonical histone marks in terminally mature cells. However, we failed to detect H3K27ac-marked regions in villus goblet cells or CD24^{hi} crypt EE cells beyond those present in Sec-Pro. Alternatively, enhancers might be active without the histone modifications we tested, so long as TFs can bind, especially in short-lived post-mitotic cells where bookmarking of enhancers (Kadauke and Blobel, 2013) may be unnecessary. Many active ESC enhancers also have open chromatin but lack H3K27ac (Pradeepa et al., 2016). A third, intriguing possibility is that weak histone marks at group 3 enhancers account for their instability and lower the barrier for specified Sec cells to dedifferentiate.

Transcripts for FEV, FLI1, RUNX, and other Ets-family TFs are selectively expressed and abundant in Sec-Pro, *Bmi1*^{Gfp}, and CD69^{+}CD274^{+} cells, and sequence motifs for these TFs are enriched at group 3 enhancers. This convergence of information from chromatin and mRNA profiles implicates these TFs in Sec differentiation. The same TFs are implicated in pancreatic endocrine cell differentiation (Gross et al., 2016) and control related processes in secretory blood cells (Ciau-Uitz et al., 2013). Thus, intestinal Sec cells may have evolved by co-opting functional modules from an ancestral anti-microbial cell, and Ets-family TFs may enable the necessary lineage-restricted chromatin access.

The RNA profile of *Bmi1*^{Gfp} cells, coupled with their absence in *Atoh1*$^{-/-}$ intestines, identifies them as EE cells rather than cells dedicated to replenishing ISCs. Several hormone mRNA levels are nearly as high as in CD24^{+} EE cells, further implying that they constitute a mature, preterminal EE population. Carcinoid tumors in humans are indolent EE malignancies often associated with clinical syndromes of hormone excess. The cells we identify with high expression of *Bmi1*, EE-restricted TFs, and gut hormones may represent the murine equivalent of crypt cells that give rise to carcinoid tumors. This idea matches with evidence that human carcinoid tumors arise in cells with *BMI1* levels modestly higher than in surrounding crypt cells (Sei et al., 2016).

Bmi1^{Gfp} cells in mice resemble (and may be a subset of) the label-retaining cells that differentiate predominantly into Paneth cells, but also into EE cells (Buczacki et al., 2013; Li et al., 2016).

Surface expression of CD69 and CD274 marks a third Sec population, which may include some Bmi^{hi} cells and LRCs but mainly contains immature goblet cells. Thus, different approaches have identified precursors for all three major Sec cell types: goblet, EE, and Paneth. It is likely significant that each of these precursors resides close to ISCs, in crypt tiers where the Ent and Sec lineages diverge as cells exit the ISC compartment. On the one hand, chromatin profiles suggest that Ent-Pros might face a lower barrier to dedifferentiate into ISCs than Sec cells. On the other hand, the magnitude of mRNA (Figure 3) and chromatin (Figure 6) shifts in dedifferentiating *Bmi1*^{Gfp} and CD69^{+}CD274^{+} cells suggests adaptation of a large fraction of cells. Taken together, the observations suggest that Ent or Sec cells closest to ISCs may be best positioned to perceive ISC deficiency and dedifferentiate in response.

In summary, we show that *Bmi1*^{Gfp} and CD69^{+}CD274^{+} cells are preterminal EE and goblet cells, respectively, that revert to the ISC state when native ISCs are depleted. Our findings also reveal a coherent basis for efficient conversion of lineage-specified crypt cells into ISCs. The distinctive properties of Lgr5^{+} ISCs and the Sec lineage may largely reflect differential chromatin access at group 3 enhancers, which relinquish this access under conditions of ISC loss.

STAR★METHODS

Detailed methods are provided in the online version of this paper and include the following:

- KEY RESOURCES TABLE
- CONTACT FOR REAGENT AND RESOURCE SHARING
- EXPERIMENTAL MODEL AND SUBJECT DETAILS
  - Mice
- METHOD DETAILS
  - Mouse treatments
  - Purification of intestinal epithelial cells
  - Detection of proteins
  - RNA-seq
  - ATAC-seq
  - ChIP-seq
- QUANTIFICATION AND STATISTICAL ANALYSIS
  - Computational analyses
  - Modeling of lineage trajectories
- DATA AND SOFTWARE AVAILABILITY

SUPPLEMENTAL INFORMATION

Supplemental Information includes six figures and two tables and can be found with this article online at http://dx.doi.org/10.1016/j.stem.2017.05.001.

AUTHOR CONTRIBUTIONS

U.J. and R.A.S. designed the study. U.J., M.S., Z.H., and K.M. acquired data. U.J., N.K.O., A.S., and G.-C.Y. performed computational analyses. R.A.S. interpreted data and supervised the study. U.J. and R.A.S. wrote the paper, with input from all authors.

ACKNOWLEDGMENTS

This work was supported by the Intestinal Stem Cell Consortium (grant U01DK103152) of the NIDDK and NIAID; NIH awards R01DK081113 (R.A.S. and G.-C.Y.), F32DK103453 (U.J.), and P50CA127003; and gifts from the Neuroendocrine Tumor Research Foundation and Pan-Mass Challenge. We thank F. de Sauvage, T. Honjo, and S. Robine for generously sharing *Lgr5*$^{Dtr\text{-}Gfp}$, *Rbpj*^{Fl}, and *Villin-Cre*$^{ER\text{-}T2}$ mice and Myles Brown, Manasvi Shah, Calvin Kuo, and David Breault for valuable discussions.

Received: August 30, 2016
Revised: February 21, 2017
Accepted: May 4, 2017
Published: June 22, 2017

SUPPORTING CITATIONS

The following references appear in the Supplemental Information: San Roman et al. (2015).

REFERENCES

Anders, S., Pyl, P.T., and Huber, W. (2015). HTSeq–a Python framework to work with high-throughput sequencing data. Bioinformatics *31*, 166–169.

Barker, N. (2014). Adult intestinal stem cells: critical drivers of epithelial homeostasis and regeneration. Nat. Rev. Mol. Cell Biol. *15*, 19–33.

Barker, N., van Es, J.H., Kuipers, J., Kujala, P., van den Born, M., Cozijnsen, M., Haegebarth, A., Korving, J., Begthel, H., Peters, P.J., and Clevers, H. (2007). Identification of stem cells in small intestine and colon by marker gene Lgr5. Nature *449*, 1003–1007.

Buczacki, S.J., Zecchini, H.I., Nicholson, A.M., Russell, R., Vermeulen, L., Kemp, R., and Winton, D.J. (2013). Intestinal label-retaining cells are secretory precursors expressing Lgr5. Nature *495*, 65–69.

Buenrostro, J.D., Giresi, P.G., Zaba, L.C., Chang, H.Y., and Greenleaf, W.J. (2013). Transposition of native chromatin for fast and sensitive epigenomic profiling of open chromatin, DNA-binding proteins and nucleosome position. Nat. Methods *10*, 1213–1218.

Ciau-Uitz, A., Wang, L., Patient, R., and Liu, F. (2013). ETS transcription factors in hematopoietic stem cell development. Blood Cells Mol. Dis. *51*, 248–255.

el Marjou, F., Janssen, K.P., Chang, B.H., Li, M., Hindie, V., Chan, L., Louvard, D., Chambon, P., Metzger, D., and Robine, S. (2004). Tissue-specific and inducible Cre-mediated recombination in the gut epithelium. Genesis *39*, 186–193.

Gross, S., Garofalo, D.C., Balderes, D.A., Mastracci, T.L., Dias, J.M., Perlmann, T., Ericson, J., and Sussel, L. (2016). The novel enterochromaffin marker Lmx1a regulates serotonin biosynthesis in enteroendocrine cell lineages downstream of Nkx2.2. Development *143*, 2616–2628.

Hama, H., Kurokawa, H., Kawano, H., Ando, R., Shimogori, T., Noda, H., Fukami, K., Sakaue-Sawano, A., and Miyawaki, A. (2011). Scale: a chemical approach for fluorescence imaging and reconstruction of transparent mouse brain. Nat. Neurosci. *14*, 1481–1488.

Han, H., Tanigaki, K., Yamamoto, N., Kuroda, K., Yoshimoto, M., Nakahata, T., Ikuta, K., and Honjo, T. (2002). Inducible gene knockout of transcription factor recombination signal binding protein-J reveals its essential role in T versus B lineage decision. Int. Immunol. *14*, 637–645.

Heintzman, N.D., Hon, G.C., Hawkins, R.D., Kheradpour, P., Stark, A., Harp, L.F., Ye, Z., Lee, L.K., Stuart, R.K., Ching, C.W., et al. (2009). Histone modifications at human enhancers reflect global cell-type-specific gene expression. Nature *459*, 108–112.

Heinz, S., Benner, C., Spann, N., Bertolino, E., Lin, Y.C., Laslo, P., Cheng, J.X., Murre, C., Singh, H., and Glass, C.K. (2010). Simple combinations of lineage-determining transcription factors prime cis-regulatory elements required for macrophage and B cell identities. Mol. Cell *38*, 576–589.

Hosen, N., Yamane, T., Muijtjens, M., Pham, K., Clarke, M.F., and Weissman, I.L. (2007). Bmi-1-green fluorescent protein-knock-in mice reveal the dynamic regulation of bmi-1 expression in normal and leukemic hematopoietic cells. Stem Cells *25*, 1635–1644.

Itzkovitz, S., Lyubimova, A., Blat, I.C., Maynard, M., van Es, J., Lees, J., Jacks, T., Clevers, H., and van Oudenaarden, A. (2011). Single-molecule transcript

counting of stem-cell markers in the mouse intestine. Nat. Cell Biol. *14*, 106–114.

Kadauke, S., and Blobel, G.A. (2013). Mitotic bookmarking by transcription factors. Epigenetics Chromatin *6*, 6.

Kim, T.H., Li, F., Ferreiro-Neira, I., Ho, L.L., Luyten, A., Nalapareddy, K., Long, H., Verzi, M., and Shivdasani, R.A. (2014). Broadly permissive intestinal chromatin underlies lateral inhibition and cell plasticity. Nature *506*, 511–515.

Langmead, B., and Salzberg, S.L. (2012). Fast gapped-read alignment with Bowtie 2. Nat. Methods *9*, 357–359.

Lara-Astiaso, D., Weiner, A., Lorenzo-Vivas, E., Zaretsky, I., Jaitin, D.A., David, E., Keren-Shaul, H., Mildner, A., Winter, D., Jung, S., et al. (2014). Immunogenetics. Chromatin state dynamics during blood formation. Science *345*, 943–949.

Li, H.J., Kapoor, A., Giel-Moloney, M., Rindi, G., and Leiter, A.B. (2012). Notch signaling differentially regulates the cell fate of early endocrine precursor cells and their maturing descendants in the mouse pancreas and intestine. Dev. Biol. *371*, 156–169.

Li, N., Yousefi, M., Nakauka-Ddamba, A., Jain, R., Tobias, J., Epstein, J.A., Jensen, S.T., and Lengner, C.J. (2014). Single-cell analysis of proxy reporter allele-marked epithelial cells establishes intestinal stem cell hierarchy. Stem Cell Reports *3*, 876–891.

Li, N., Nakauka-Ddamba, A., Tobias, J., Jensen, S.T., and Lengner, C.J. (2016). Mouse label-retaining cells are molecularly and functionally distinct from reserve intestinal stem cells. Gastroenterology *151*, 298–310.

Love, M.I., Huber, W., and Anders, S. (2014). Moderated estimation of fold change and dispersion for RNA-seq data with DESeq2. Genome Biol. *15*, 550.

McLean, C.Y., Bristor, D., Hiller, M., Clarke, S.L., Schaar, B.T., Lowe, C.B., Wenger, A.M., and Bejerano, G. (2010). GREAT improves functional interpretation of cis-regulatory regions. Nat. Biotechnol. *28*, 495–501.

Mercer, T.R., Edwards, S.L., Clark, M.B., Neph, S.J., Wang, H., Stergachis, A.B., John, S., Sandstrom, R., Li, G., Sandhu, K.S., et al. (2013). DNase I-hypersensitive exons colocalize with promoters and distal regulatory elements. Nat. Genet. *45*, 852–859.

Metcalfe, C., Kljavin, N.M., Ybarra, R., and de Sauvage, F.J. (2014). Lgr5+ stem cells are indispensable for radiation-induced intestinal regeneration. Cell Stem Cell *14*, 149–159.

Muñoz, J., Stange, D.E., Schepers, A.G., van de Wetering, M., Koo, B.K., Itzkovitz, S., Volckmann, R., Kung, K.S., Koster, J., Radulescu, S., et al. (2012). The Lgr5 intestinal stem cell signature: robust expression of proposed quiescent '+4' cell markers. EMBO J. *31*, 3079–3091.

Pelaseyed, T., Bergström, J.H., Gustafsson, J.K., Ermund, A., Birchenough, G.M., Schütte, A., van der Post, S., Svensson, F., Rodríguez-Piñeiro, A.M., Nyström, E.E., et al. (2014). The mucus and mucins of the goblet cells and enterocytes provide the first defense line of the gastrointestinal tract and interact with the immune system. Immunol. Rev. *260*, 8–20.

Pinello, L., Xu, J., Orkin, S.H., and Yuan, G.C. (2014). Analysis of chromatin-state plasticity identifies cell-type-specific regulators of H3K27me3 patterns. Proc. Natl. Acad. Sci. USA *111*, E344–E353.

Potten, C.S. (1998). Stem cells in gastrointestinal epithelium: numbers, characteristics and death. Philos. Trans. R. Soc. Lond. B Biol. Sci. *353*, 821–830.

Pradeepa, M.M., Grimes, G.R., Kumar, Y., Olley, G., Taylor, G.C., Schneider, R., and Bickmore, W.A. (2016). Histone H3 globular domain acetylation identifies a new class of enhancers. Nat. Genet. *48*, 681–686.

Quinlan, A.R., and Hall, I.M. (2010). BEDTools: a flexible suite of utilities for comparing genomic features. Bioinformatics *26*, 841–842.

Ramírez, F., Dündar, F., Diehl, S., Grüning, B.A., and Manke, T. (2014). deepTools: a flexible platform for exploring deep-sequencing data. Nucleic Acids Res. *42*, W187–W191.

Richmond, C.A., Shah, M.S., Carlone, D.L., and Breault, D.T. (2016). An enduring role for quiescent stem cells. Dev. Dyn. *245*, 718–726.

Robinson, J.T., Thorvaldsdóttir, H., Winckler, W., Guttman, M., Lander, E.S., Getz, G., and Mesirov, J.P. (2011). Integrative genomics viewer. Nat. Biotechnol. *29*, 24–26.

San Roman, A.K., Tovaglieri, A., Breault, D.T., and Shivdasani, R.A. (2015). Distinct Processes and Transcriptional Targets Underlie CDX2 Requirements in Intestinal Stem Cells and Differentiated Villus Cells. Stem Cell Reports *5*, 673–681.

Sangiorgi, E., and Capecchi, M.R. (2008). Bmi1 is expressed in vivo in intestinal stem cells. Nat. Genet. *40*, 915–920.

Schindelin, J., Arganda-Carreras, I., Frise, E., Kaynig, V., Longair, M., Pietzsch, T., Preibisch, S., Rueden, C., Saalfeld, S., Schmid, B., et al. (2012). Fiji: an open-source platform for biological-image analysis. Nat. Methods *9*, 676–682.

Schwitalla, S., Fingerle, A.A., Cammareri, P., Nebelsiek, T., Göktuna, S.I., Ziegler, P.K., Canli, O., Heijmans, J., Huels, D.J., Moreaux, G., et al. (2013). Intestinal tumorigenesis initiated by dedifferentiation and acquisition of stem-cell-like properties. Cell *152*, 25–38.

Sei, Y., Feng, J., Zhao, X., Forbes, J., Tang, D., Nagashima, K., Hanson, J., Quezado, M.M., Hughes, M.S., and Wank, S.A. (2016). Polyclonal Crypt Genesis and Development of Familial Small Intestinal Neuroendocrine Tumors. Gastroenterology *151*, 140–151.

Shlyueva, D., Stampfel, G., and Stark, A. (2014). Transcriptional enhancers: from properties to genome-wide predictions. Nat. Rev. Genet. *15*, 272–286.

Shroyer, N.F., Helmrath, M.A., Wang, V.Y., Antalffy, B., Henning, S.J., and Zoghbi, H.Y. (2007). Intestine-specific ablation of mouse atonal homolog 1 (Math1) reveals a role in cellular homeostasis. Gastroenterology *132*, 2478–2488.

Subramanian, A., Tamayo, P., Mootha, V.K., Mukherjee, S., Ebert, B.L., Gillette, M.A., Paulovich, A., Pomeroy, S.L., Golub, T.R., Lander, E.S., and Mesirov, J.P. (2005). Gene set enrichment analysis: a knowledge-based approach for interpreting genome-wide expression profiles. Proc. Natl. Acad. Sci. USA *102*, 15545–15550.

Takeda, N., Jain, R., LeBoeuf, M.R., Wang, Q., Lu, M.M., and Epstein, J.A. (2011). Interconversion between intestinal stem cell populations in distinct niches. Science *334*, 1420–1424.

Tetteh, P.W., Basak, O., Farin, H.F., Wiebrands, K., Kretzschmar, K., Begthel, H., van den Born, M., Korving, J., de Sauvage, F., van Es, J.H., et al. (2016). Replacement of lost Lgr5-positive stem cells through plasticity of their enterocyte-lineage daughters. Cell Stem Cell *18*, 203–213.

Tian, H., Biehs, B., Warming, S., Leong, K.G., Rangell, L., Klein, O.D., and de Sauvage, F.J. (2011). A reserve stem cell population in small intestine renders Lgr5-positive cells dispensable. Nature *478*, 255–259.

Trapnell, C., Roberts, A., Goff, L., Pertea, G., Kim, D., Kelley, D.R., Pimentel, H., Salzberg, S.L., Rinn, J.L., and Pachter, L. (2012). Differential gene and transcript expression analysis of RNA-seq experiments with TopHat and Cufflinks. Nat. Protoc. *7*, 562–578.

van Es, J.H., van Gijn, M.E., Riccio, O., van den Born, M., Vooijs, M., Begthel, H., Cozijnsen, M., Robine, S., Winton, D.J., Radtke, F., and Clevers, H. (2005). Notch/gamma-secretase inhibition turns proliferative cells in intestinal crypts and adenomas into goblet cells. Nature *435*, 959–963.

van Es, J.H., Sato, T., van de Wetering, M., Lyubimova, A., Nee, A.N., Gregorieff, A., Sasaki, N., Zeinstra, L., van den Born, M., Korving, J., et al. (2012). Dll1+ secretory progenitor cells revert to stem cells upon crypt damage. Nat. Cell Biol. *14*, 1099–1104.

Verzi, M.P., Shin, H., He, H.H., Sulahian, R., Meyer, C.A., Montgomery, R.K., Fleet, J.C., Brown, M., Liu, X.S., and Shivdasani, R.A. (2010). Differentiation-specific histone modifications reveal dynamic chromatin interactions and partners for the intestinal transcription factor CDX2. Dev. Cell *19*, 713–726.

Westphalen, C.B., Asfaha, S., Hayakawa, Y., Takemoto, Y., Lukin, D.J., Nuber, A.H., Brandtner, A., Setlik, W., Remotti, H., Muley, A., et al. (2014). Long-lived intestinal tuft cells serve as colon cancer-initiating cells. J. Clin. Invest. *124*, 1283–1295.

Wong, V.W., Stange, D.E., Page, M.E., Buczacki, S., Wabik, A., Itami, S., van de Wetering, M., Poulsom, R., Wright, N.A., Trotter, M.W., et al. (2012). Lrig1 controls intestinal stem-cell homeostasis by negative regulation of ErbB signalling. Nat. Cell Biol. *14*, 401–408.

Yan, K.S., Chia, L.A., Li, X., Ootani, A., Su, J., Lee, J.Y., Su, N., Luo, Y., Heilshorn, S.C., Amieva, M.R., et al. (2012). The intestinal stem cell markers Bmi1 and Lgr5 identify two functionally distinct populations. Proc. Natl. Acad. Sci. USA *109*, 466–471.

Yang, Q., Bermingham, N.A., Finegold, M.J., and Zoghbi, H.Y. (2001). Requirement of Math1 for secretory cell lineage commitment in the mouse intestine. Science *294*, 2155–2158.

Zhang, Y., Liu, T., Meyer, C.A., Eeckhoute, J., Johnson, D.S., Bernstein, B.E., Nusbaum, C., Myers, R.M., Brown, M., Li, W., and Liu, X.S. (2008). Model-based analysis of ChIP-Seq (MACS). Genome Biol. *9*, R137.

Zhu, C., Chen, Z., and Jiang, Z. (2016). Expression, distribution and role of aquaporin water channels in human and animal stomach and intestines. Int. J. Mol. Sci. *17*, 17.

STAR★METHODS

KEY RESOURCES TABLE

REAGENT or RESOURCE	SOURCE	IDENTIFIER
Antibodies		
CD69-BV421	BD Biosciences	Cat#562920
CD69	eBioscience	Cat#564715; RRID: AB_467324
CD69	R&D Systems	Cat#AF2386; RRID: AB_416586
CD274-APC	BD Biosciences	Cat#564715
CD274	Bio-Rad	Cat#MCA2626; AB_1125243
CD24-Alexa Fluor 647	BioLegend	Cat#101818; RRID: AB_493484
BrdU	Bio-Rad	Cat#OBT0030; RRID: AB_609568
GFP	Santa Cruz	Cat#SC9996; RRID: AB_627695
EPCAM-FITC	eBioscience	Cat#11-5791-82; RRID: AB_11151709
EPCAM-APC	eBioscience	Cat#17-5791-80; RRID: AB_1659714
H3K4me1	Diagenode	Cat#C15410194
H3K4me2	Millipore	Cat#07-030; RRID: AB_11213050
H3K27Ac	Active Motif	Cat#39135; RRID: AB_2614979
FEV	Santa Cruz	Cat#sc-6530X
CHGA	Abcam	Cat#ab15160; RRID: AB_301704
Chemicals, Peptides, and Recombinant Proteins		
TrypLE Select Enzyme (10X)	ThermoFisher	A1217702
Diphtheria toxin	Sigma-Aldrich	D0564
Trizol reagent	ThermoFisher	15596026
High-Fidelity 2X PCR master mix	New England Biolabs	M0541S
Agencourt AMPure XP beads	Beckman Coulter	A63881
Micrococcal nuclease	Sigma-Aldrich	N3755
cOmplete, mini protease inhibitor cocktail	Sigma-Aldrich	11836153001
Dispase	Stem Cell Technologies	07913
Ulex europaeus lectin- Atto 488	Sigma-Aldrich	Cat#19337
Dibenzazepine (DBZ)	Syncom	SIC-020042
Critical Commercial Assays		
RNase-Free DNase Set	QIAGEN	Cat# 79254
SMART-Seq v4 Ultra Low Input RNA Kit	Clontech	634890
Nextera DNA Library Preparation Kit	Illumina	FC-121-1030
Qubit dsDNA HS Assay Kit	Thermo Fisher Scientific	Q32854
E-Gel Precast Agarose Electrophoresis System	ThermoFisher	G661002
ThruPLEX DNA-seq 48S Kit	Rubicon Genomics	R400427
Elite ABC Kit	Vector	PK-6100
Vectastain ABC-AP Kit	Vector	AK-5000
MinElute PCR Purification Kit	QIAGEN	28004
Deposited Data		
Raw and analyzed data	This paper	Table S1; GEO: GSE83394
Mouse reference genome Mm10, GRCm38	Genome Reference Consortium	https://www.ncbi.nlm.nih.gov/grc/mouse
Experimental Models: Organisms/Strains		
Mouse: *Lgr5*$^{Cre\text{-}Gfp}$	The Jackson Laboratory	008875
Mouse: *Atoh1*$^{Fl/Fl}$	The Jackson Laboratory	008681
Mouse: *Bmi1*^{Gfp}	The Jackson Laboratory	017351
Mouse: *Lgr5*$^{Dtr\text{-}Gfp}$	(Tian et al., 2011)	N/A

(*Continued on next page*)

Continued		
REAGENT or RESOURCE	SOURCE	IDENTIFIER
Mouse: *Villin*$^{CreER-T2}$	(Han et al., 2002)	N/A
Mouse: *Rbpj*$^{Fl/Fl}$	(el Marjou et al., 2004)	N/A
Oligonucleotides		
Oligonucleotides	This paper	Table S2
Software and Algorithms		
TopHat v2.0.6	(Trapnell et al., 2012)	https://ccb.jhu.edu/software/tophat/index.shtml
Bowtie2	(Langmead and Salzberg, 2012)	http://bowtie-bio.sourceforge.net/bowtie2/index.shtml
HTSeq	(Anders et al., 2015)	https://github.com/simon-anders/htseq
DEseq2	(Love et al., 2014)	https://bioconductor.org/packages/release/bioc/html/DESeq2.html
MACS v1.4	(Zhang et al., 2008)	http://liulab.dfci.harvard.edu/MACS/
DeepTools v2.1.0	(Ramírez et al., 2014)	https://github.com/fidelram/deepTools
GREAT	(McLean et al., 2010)	http://bejerano.stanford.edu/great/public/html/
Bedtools	(Quinlan and Hall, 2010)	http://bedtools.readthedocs.io/en/latest/
Integrated Genomics Viewer	(Robinson et al., 2011)	http://software.broadinstitute.org/software/igv/
HOMER v4.7.2	(Heinz et al., 2010)	http://homer.ucsd.edu/homer/
Gene Set Enrichment Analysis (GSEA)	(Subramanian et al., 2005)	http://software.broadinstitute.org/gsea/index.jsp
GENE-E	Broad Institute	https://software.broadinstitute.org/GENE-E/

CONTACT FOR REAGENT AND RESOURCE SHARING

Requests should be directed to, and will be fulfilled by, the Lead Contact, Ramesh Shivdasani (ramesh_shivdasani@dfci.harvard.edu) after execution of a suitable Materials Transfer Agreement.

EXPERIMENTAL MODEL AND SUBJECT DETAILS

Mice

All mouse strains used in this study (*Bmi*^{Gfp}, *Lgr5*$^{Cre-Gfp}$, *Lgr5*$^{Dtr-Gfp}$, *Rbpj*$^{Fl/Fl}$;*Villin*$^{CreER-T2}$, *Atoh1*$^{Fl/Fl}$;*Villin*$^{CreER-T2}$) were maintained on a mixed C57BL/6 and 129/Sv background. Animals were housed in a Specific Pathogen-Free environment in 12 hr light/dark cycles with room temperature at 23 ± 1° C and humidity at 55 ± 15%. Food and water were available *ad libitum*. Animals were weaned 21 days after birth and handled and euthanized according to protocols approved by the Animal Care and Use Committee of the Dana-Farber Cancer Institute. Mice were at least 8 weeks old at the time of experimental treatments and cell isolations. Mice of both sexes were used in all experiments and littermates were used as controls.

METHOD DETAILS

Mouse treatments

Bmi^{Gfp} mice received 10 Gy whole-body γ-irradiation 24 hr or 36 hr before euthanasia. To ablate ISC in *Lgr5*$^{Dtr-Gfp}$ mice, we administered intraperitoneal (i.p.) *Diphtheria* toxin (Sigma-Aldrich, 50 μg/kg) every other day and harvested intestines 24 hr after the 4th dose. To enrich Ent-Pro, we injected *Atoh1*$^{Fl/Fl}$;*Villin*$^{CreER-T2}$ mice daily with 1 mg tamoxifen for 5 days and waited > 4 weeks to eliminate Sec cells. Mice were genotyped by PCR before weaning and the genotypes of all experimental animals were confirmed by repeat PCR.

To enrich Sec-Pro and goblet cells, we treated wild-type mice twice 12 hr apart with the Notch inhibitor dibenzazepine (DBZ, 48 mg/kg). About 38 hr after the first dose, we harvested intestines and scraped off villi using glass slides. The crypt-enriched tissue was rotated in 5 mM EDTA (pH 8) in phosphate-buffered saline (PBS) at 4°C for 45 min. The tissue was manually shaken every 10 min and the EDTA solution was changed once after 30 min. Remaining villi were filtered out using 70-μm filter and crypts enriched for Sec-Pro were pelleted by centrifugation at 130*g* at 4° C. To isolate goblet cells, we collected villi 115 hr after wild-type mice were treated with DBZ as above, by shaking intestines gently in 5 mM EDTA for 30 min at 4°C, followed by elimination of crypts by passing through 70 um filters.

For an alternative means to enrich Sec-Pro, we injected *Rbpj*$^{Fl/Fl}$;*Villin*$^{CreER-T2}$ mice 4 times with 2 mg tamoxifen over 2 days, harvested crypts on day 3, and processed the tissue as described above for DBZ-treated animals. To detect proliferating cells, we collected intestines 1 hr after injecting mice i.p. with 1 mg BrdU in PBS.

Purification of intestinal epithelial cells

Cells were isolated from the proximal 1/3 small intestine. After scraping villi using a glass slide, intestines were rinsed, then rotated in 5 mM EDTA (pH 8) in PBS at 4°C for 45 min, with manual shaking every 10 min and a change of solution after 30 min. Released crypts were passed through a 70-μm strainer to eliminate villi and dissociated into single cells by rotating in 4% TrypLE solution (ThermoFisher) at 37°C for 30-45 min. GFP$^+$ cells from *Lgr5$^{Cre\text{-}Gfp}$*, *Lgr5$^{Dtr\text{-}Gfp}$*, and *Bmi^{Gfp}* mice were isolated on a FACSAria II SORP flow cytometer. To isolate CD69$^+$CD274$^+$ cells, single-cell suspensions were labeled with BV421-conjugated CD69 Ab (BD Biosciences 562920) and APC-conjugated CD274 Ab (BD Biosciences 564715). Dead cells were eliminated using DAPI for all flow cytometry isolations. Live epithelial cells staining with FITC-conjugated EPCAM (eBioscience, 11-5791-82) and CD69 or CD274 Ab were used to identify the signal range and to gate for FACS sorting of live CD69$^+$CD274$^+$ cells.

To isolate CD24^{hi}UEA^{hi} Paneth cells and CD24^{hi}UEA$^-$ EE cells, crypts were dissociated by rotating in DMEM containing 0.5 U/ml Dispase (Stem Cell Technologies) at 37°C for 30 min (Wong et al., 2012). Cells were labeled with Alexa Fluor 647-conjugated CD24 antibody (BioLegend) and Atto 488-conjugated *Ulex europaeus* lectin (Sigma-Aldrich) at 4°C for 30 min, followed by flow cytometry.

Detection of proteins

To detect GFP$^+$ cells, *Lgr5^{Gfp}* and *Bmi1^{Gfp}* mouse duodeni were fixed in 4% paraformaldehyde for 40 min, washed in PBS, and cleared by shaking in ScaleA2 solution (4 M Urea, 0.1% Triton X-100 and 10% glycerol) (Hama et al., 2011) for 45 min. Crypts were visualized using a Zeiss LSM710 laser scanning microscope, and data were analyzed using Zen2009 (Zeiss) and Fiji software (Schindelin et al., 2012). For immunohistochemistry, 5 μm wax sections of paraformaldehyde-fixed intestines were deparaffinized, rehydrated, treated with 10 mM sodium citrate buffer (pH 6) to retrieve antigens, and incubated overnight at 4°C with Ab against FEV (Santa Cruz sc-6530X, 1:200), CD69 (eBioscience 14-0691-81, 1:500) or CD274 (Bio-Rad MCA2626, 1:500), all diluted in PBS. FEV, CD69, and CD274 were detected using biotin-conjugated anti-goat, anti-hamster or anti-rat IgG (Jackson Laboratories, 1:1000). Reactions were completed using Vectastain Elite ABC Kit (Vector) and 3,3′ diaminobenzidine tetrahydrochloride (Sigma P8375, brown stain) or Vectastain ABC-AP Kit (Vector, blue stain). To co-localize markers, antigen-retrieved tissue sections were exposed to CD69 (R&D Systems AF2386, 1:500), CD274 (Bio-Rad MCA2626, 1:500), BrdU (Bio-Rad OBT0030CX), and/or GFP (Santa Cruz, SC9996) Ab in various combinations, followed by anti-goat, -rat or -mouse secondary Ab conjugated with Alexa Fluor 488, 546 or 647. Serial sections were used to identify BrdU$^+$ replicating CD69$^+$CD274$^+$ cells. To localize CHGA in *Bmi1^{Gfp}* mice, fixed intestines were flash-frozen in OCT compound (Tissue-Tek, 4583) and 5 μm sections were stained with CHGA Ab (Abcam ab15160, 1:100) and Cy3-conjugated anti-rabbit IgG.

RNA-seq

Lgr5$^+$ ISC, *Bmi1^{Gfp}*, EE, Paneth, goblet, and CD69$^+$CD274$^+$ cells were collected by FACS directly in Trizol reagent (ThermoFisher); RNA from Sec- and Ent-Pro was also purified using Trizol. RNA isolates were treated with DNase (QIAGEN) to remove contaminating DNA. Total RNA (5 to 10 ng) was used to prepare libraries with the SMART-Seq v4 Ultra Low Input RNA Kit (Clontech) following the manufacturer's protocol.

ATAC-seq

We performed ATAC-seq (Buenrostro et al., 2013) on replicate samples of 8,000 to 35,000 cells washed twice in ice-cold PBS. Cells were resuspended in 50 μl ice-cold ATAC lysis buffer (10 mM Tris·Cl, pH 7.4, 10 mM NaCl, 3 mM MgCl2, 0.1% (v/v) Igepal CA-630) and centrifuged at 500 g at 4°C to isolate nuclear pellets that we treated in 50 μL reactions with Nextera Tn5 Transposase (Illumina, FC-121-1030) for 30 min at 37°C. Column-purified DNA (QIAGEN) was stored at −20°C or amplified immediately in 50 μl reactions with high-fidelity 2X PCR Master Mix (New England Biolabs) using a common forward primer and different reverse primers with unique barcodes for each sample. From the reaction mix, 45 μl was kept on ice after 5 cycles of PCR, while 5 μl was amplified by qPCR for 20 additional cycles; the remaining 45 μl was then amplified for the 5-7 cycles required to achieve 1/3 of the maximum qPCR fluorescence intensity. Amplified DNA was purified over columns and primer dimers (< 100 bp) were removed using AMPure beads (Beckman Coulter). Size distribution of the amplified DNA was analyzed using High-sensitivity Qubit dsDNA Assay Kit (ThermoFisher).

ChIP-seq

For H3K4me1 ChIP-seq, Ent-Pro and Sec-Pro crypts were fixed immediately after isolation by rotating in in 1% formaldehyde for 25 min at room temperature. Fixed crypts were lysed in buffer containing 1% SDS, 10 mM EDTA, 30 mM Tris-HCl pH 8, with protease inhibitors (Roche). Lysates were sonicated using a Covaris E210 sonicator for 50 min with 5 min on/off cycles at 4°C and debris were removed by centrifugation. The resulting chromatin was flash frozen and preserved at −80°C or used immediately for ChIP. For H3K4me2 and H3K27ac, cells were treated with 0.2 U micrococcal nuclease (Sigma, N3755) in buffer containing 50 mM Tris-HCl (pH7.6), 1 mM $CaCl_2$, 0.2% Triton X-100, protease inhibitors (Roche), and 0.5 mM phenyl methyl sulfonyl fluoride (PMSF) at 37°C for 6 min, followed by dialysis against RIPA buffer (50 mM HEPES (pH 7.6), 1 mM EDTA, 0.7% Na deoxycholate, 1% NP-40, 0.5 M LiCl) for 3 hr at 4°C. Chromatin was isolated by centrifugation and incubated overnight at 4°C with well-validated ChIP-grade Ab against H3K4me1 (Diagenode, C15410194), H3K4me2 (Millipore, 07-030) or H3K27Ac (Active Motif, 39135), followed by capture with magnetic beads (Dynal) that we washed 4 times in RIPA buffer and twice in 1 mM EDTA in 10 mM Tris-HCL, pH 8. Cross-links were reversed using 1% SDS and 0.1 M NaHCO3 for 6 hr at 65°C. DNA was purified using a kit (QIAGEN) or by isolating the

mononucleosome fraction in 2% E-gels (Invitrogen). Libraries were prepared using ThruPLEX kits (Rubicon, R400427), and DNA size distribution was confirmed using High-sensitivity Qubit dsDNA Assay Kit (ThermoFisher).

All libraries (RNA-seq, ATAC-seq, and ChIP-seq) were sequenced on a NextSeq 500 instrument (Illumina) to obtain 75 bp single-end reads.

QUANTIFICATION AND STATISTICAL ANALYSIS

Given the potential variability among animals and low abundance of *Bmi1*^{Gfp} and CD69^{+}CD274^{+} cells, all immunohistochemistry (Figure 5C) and immunofluorescence (Figures 2A and 3B) studies used tissue from at least 3 independent animals (N = 3). Similarly, in co-localization studies to illustrate the endocrine phenotype of *Bmi1*^{Gfp} cells (Figure 1G) we interrogated large number of cells (N = 165). To ensure reproducibility of purification methods for *Bmi1*^{Gfp} and CD69^{+}CD274^{+} cells by flow cytometry, all experiments involving FACS occurred on at least 3 and as many as 9 individual animals (N = 3 to 9, Figures 2A, 2B, 2D, S1G, S2B, and S3B). For consistency in analysis and representation, FACS data from 50,000 cells were analyzed in every experiment using FlowJo v10 software (FlowJo LLC).

To confirm cell purity achieved in our isolation approaches, and to exclude potential biases introduced by RNA-seq library preparation, sequencing and data processing, we conducted semiquantitative RT-PCR analysis on mRNAs from three independent animal samples (N = 3) using primers for cell-specific markers (Figure S2B) and confirmed relative enrichment of known lineage markers. Similarly, we confirmed expression changes revealed by RNA-seq in *Bmi1*^{Gfp} and CD69^{+}CD274^{+} cells upon Lgr5^{+} ISC ablation by RT-PCR analysis of RNA samples from at least three independent (N = 3) animals, using whole crypts (Figures 3B and S3E) or ISC (Figures 3G and S3F) to determine basal expression.

Computational analyses

Raw reads from mRNA-, ChIP-, and ATAC-seq were aligned to the mouse genome (Mm10, Genome Reference Consortium GRCm38) using TopHat v2.0.6 (Trapnell et al., 2012) or Bowtie2 (Langmead and Salzberg, 2012). For RNA-seq, transcript levels were expressed as read counts using HTSeq (Anders et al., 2015). Data were normalized and sample variability assessed by principal component analysis in DEseq2 (Love et al., 2014). Differential expression was defined using the indicated fold-changes and false-discovery rate (FDR) 0.05 using DEseq2. We used GENE-E software (Broad Institute) to generate heatmaps of RNA levels, averaged from replicate samples in reads per kb of transcript per 1M mapped reads (RPKM).

For ATAC- and ChIP-seq, aligned signals in raw (bam) files were filtered to remove PCR duplicates and reads that aligned to multiple locations; the remainder is listed in Table S1. Peaks were identified using MACS v1.4 (Zhang et al., 2008) with the p-value cut-off 10^{-5}. ATAC peaks from Lgr5^{+} ISC, Sec-Pro, Ent-Pro, *Bmi1*^{Gfp}, and CD69^{+}CD274^{+} cells were pooled and the 50,347 unique peaks were used in sample correlations (Figures 4C, S4B, 6A, and 6B). Promoters (regions < 1 kb from TSSs) were discarded, leaving 41,167 sites as candidate enhancers. Raw signals from individual samples or merged, highly correlated replicates (Figure S4B) from a given cell type were converted to signal files (bigWig) using DeepTools v2.1.0 (Ramírez et al., 2014). To compare open chromatin across cell types, signals were quantile-normalized using Haystack (Pinello et al., 2014), with 50-bp windows. Normalized signals ± 1.5 kb from center of ATAC peaks were used for unsupervised k-means clustering in DeepTools v2.1.0. The optimum number of clusters was determined by gap statistics (Figure S4C) and the 8 resulting clusters were merged, according to similarity of signal patterns, into 3 distinct groups (Figure S4D).

To determine correlations among multiple ATAC-seq samples, read counts from all samples under consideration were summarized over pooled ATAC peaks into a matrix using DeepTools. Samples were clustered using hierarchical clustering and heatmap scales reflect the full range of sample-to-sample Spearman correlation coefficients (Figures 4C, 6A, 6C, and S6). Enhancer ATAC-seq signals were determined using 50 bp bins over $\pm$1.5 kb or $\pm$3.5 kb from the center of the regions and plotted as heatmaps using DeepTools in descending order of the mean signal over $\pm$1.5 kb, as determined for each cluster in Figure 4D. The same order of sites was maintained for plotting regions from Groups 1, 2 and 3 in Figures 5A, 6B, 6D, S4D, and S5C. The same signal values were used to generate aggregate profile plots in DeepTools.

Ontologies associated with genes located within 25 kb of ATAC regions were identified using GREAT analysis v3.0 (McLean et al., 2010). To identify biological processes enriched in cell populations, we applied Gene Set Enrichment Analysis (GSEA) (Subramanian et al., 2005) to curated Biocarta, Kegg, and chemical and genetic perturbation sets from the molecular signature database (MSigDB), using default parameters. Genes within 25 kb of enhancers in Groups 2 and 3 were identified using Bedtools (Quinlan and Hall, 2010). Enriched expression of these gene sets was determined in different populations using the GSEA approach (Subramanian et al., 2005); significance of the enrichment scores (FDR) was determined using 1,000 permutations of random gene sets of similar size. Similarly, 500 transcripts with the highest enrichment in *Bmi1*^{Gfp} or CD69^{+}CD274^{+} cells were analyzed to determine specificity for Ent- or Sec-Pro and EE, Paneth or goblet cells (Figures 1F and 2D). Loci were visualized using the Integrated Genomics Viewer v2.3 (Robinson et al., 2011). Motifs enriched in ATAC regions were identified using the HOMER de novo algorithm v4.7.2 (Heinz et al., 2010) based on the cumulative binomial distribution.

Modeling of lineage trajectories

To define cell relationships, we constructed a mathematical model based on the simplifying assumption of monotonic changes, i.e., directions of change in mRNA expression are consistent from mother to daughter cells along a trajectory. For any trajectory

$A \rightarrow B \rightarrow C$, where A, B and C represent different cell populations, we defined a coherence score based on the direction of change of differentially expressed ($q < 0.05$) genes. For any gene $g \in N = diff(A,B) \cap diff(B,C) \cap diff(A,C)$, where *diff* denotes the gene set differentially expressed in two cell types, the coherence score $\delta_g = +1$ if transcript levels increase or decrease consistently along the trajectory, and as $\delta_g = -1$ otherwise. The weighted sum of δ_g's, where each gene is weighted by the magnitude of log fold-change $\left|\log FC_g^{C/A}\right|$, then gives an aggregated coherence score $= \sum_{g \in N} \left|\log FC_g^{C/A}\right| \cdot \delta_g$. High positive scores for a trajectory indicate consistency of monotonic gene expression, and negative scores reflect opposing changes in many genes, along the trajectory, e.g., the ISC → EP → Enterocyte and ISC → SP → Goblet cells trajectories gave the expected high positive scores (Figure S1F).

DATA AND SOFTWARE AVAILABILITY

The accession number for the data reported in Table S1 is GEO: GSE83394.